

“Phase-Enhanced” 3D Snapshot ISAR Imaging and Interferometric SAR

J.T. Mayhan

28 December 2009

Lincoln Laboratory
MASSACHUSETTS INSTITUTE OF TECHNOLOGY
LEXINGTON, MASSACHUSETTS



Prepared for the Missile Defense Agency under Air Force Contract FA8721-05-C-0002.

Approved for public release; distribution is unlimited.

20100105288

MIT LINCOLN LABORATORY

0028



G18D272373U

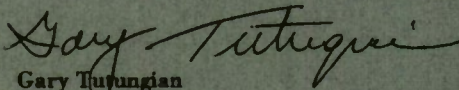
This report is based on studies performed at Lincoln Laboratory, a center for research operated by Massachusetts Institute of Technology. This work was sponsored by the Missile Defense Agency, DV, under Air Force Contract FA8721-05-C-0002.

This report may be reproduced to satisfy needs of U.S. Government agencies.

The MDA Public Affairs Office has reviewed this report, and it is releasable to the National Technical Information Service, where it will be available to the general public, including foreign nationals.

This technical report has been reviewed and is approved for publication.

FOR THE COMMANDER



Gary Tutunjian
Administrative Contracting Officer
Plans and Programs Directorate
Contracted Support Management

Non-Lincoln Recipients

PLEASE DO NOT RETURN

Permission has been given to destroy this document when it is no longer needed.

Massachusetts Institute of Technology
Lincoln Laboratory

“Phase-Enhanced” 3D Snapshot ISAR Imaging and Interferometric SAR

J.T. Mayhan
Group 32

Technical Report 1135

28 December 2009

Approved for public release; distribution is unlimited.

Lexington

Massachusetts

This page intentionally left blank.

ABSTRACT

In [1], we presented a novel formulation for the generation of three-dimensional (3D) inverse synthetic aperture radar (ISAR) images based on recent developments in high resolution spectral estimation theory. Because this technique requires only "snapshots" of data, where a "snapshot" is defined as a block of Nyquist sampled frequency-time pulses of data, we refer to it as "3D snapshot imaging." Concomitant with these results, recent advances in interferometric SAR imaging have demonstrated the use of two-dimensional (2D) range-Doppler image phase information to extract "out-of-plane" height information to obtain 3D images of ground scenes. In this case, a unique sampling grid is generated that allows "overlying" of nearly identical 2D range-Doppler images and uses phase differences between these images to estimate the "out-of-plane" height information, from which a 3D image is developed.

In this report, we develop a framework connecting these two techniques, particularly applicable to forming 3D images of target types typically dominated by smaller numbers (≤ 20) of scattering centers, and characterized by deterministic exoatmospheric motion having torque-free Euler dynamic spin and precession. For the application considered here, the 3D image is formed using the localized microdynamic changes in look angles to the target characterized by Euler's 6 Degrees-of-Freedom (6DOF) dynamical equations of motion. This type of motion allows the formation of short-time-interval range-Doppler images at nearly constant look angle K to the time invariant angular momentum vector \underline{J} . This short-time processing is contrasted with longer-time ISAR imaging of satellites, where changes in look angle to the target are obtained from changes in the long-term trajectory of the satellite.

Applications of the development are illustrated using simulation data; specifically, the wideband, monostatic field is simulated using a simple point scatter model of a generic cone-like target, and the phase-enhanced 3D image is generated for differing cases. Extensions of the technique to bistatics are also discussed.

This page intentionally left blank.

TABLE OF CONTENTS

	Page No.
Abstract	iii
List of Illustrations	vii
1. INTRODUCTION	1
2. EULER MOTION AND SAMPLING CONSIDERATIONS	3
3. DEVELOPMENT (SINGLE MONOSTATIC SENSOR)	9
4. THE GENERALIZED "PHASE-ENHANCED" SNAPSHOT IMAGING FRAMEWORK	11
5. SIMULATION	17
6. APPLICATION TO BISTATICS	23
7. SUMMARY	25
REFERENCES	27

This page intentionally left blank.

LIST OF ILLUSTRATIONS

Figure No.		Page No.
1	Motion and target scattering reference frames.	3
2	Euler motion (θ , ϕ and \hat{k} vs. time) for small precession and $f_s \gg f_p$.	6
3	IF-ISAR sampling grids.	6
4	Types of sparse-angle sampling.	7
5	Snapshot sampling: conventional vs. phase-enhanced.	8
6	Component extraction using block processing vs. conventional Fourier image.	11
7	Localized orthogonal coordinate system for 3D phase-enhanced precessing.	14
8	RV simulation geometry.	17
9	Simulation motion parameters $\theta(t)$, $\phi(t)$ and typical range-Doppler image.	18
10	$\theta(t)$ vs. $\phi(t)$ illustrated parametrically in time.	19
11	Image grid and extracted poles.	20
12	Range-Doppler pairs ($t = t_0$ vs. $t = t_q$).	21
13	Phase-enhanced 3D snapshot image.	21
14	Conventional snapshot imaging (aspect sample $>$ Nyquist).	22
15	Maximum baseline for bistatic collections.	24

This page intentionally left blank.

1. INTRODUCTION

Three-dimensional (3D) radar imaging of inverse synthetic aperture radar (ISAR) data presents a challenge of considerable importance to numerous application areas. The development and study of 3D ISAR imaging and associated effects has been carried out by various researchers [2–4]. A general formulation of this 3D imaging problem is presented in [2]. The essence of that formulation is to characterize the target by setting up a 3D grid registered in a coordinate system centered within the target, and associating two-dimensional (2D) range-Doppler image planar cuts through the target with points on this grid using the (assumed) known aspect angle to the target. When the radar samples a planar cut through the target, the resulting image will necessarily be 2D. When the radar densely samples a 3D solid angle of target aspects, a 3D image of these scatterers can be developed.

In a previous paper [1], we presented a new formulation for the generation of 3D ISAR images based on recent developments in high resolution spectral estimation theory. Because this technique requires only high resolution “snapshots” of data, we refer to it as “3D snapshot imaging.” Because of the snapshot nature of the technique, it is particularly applicable to 3D imaging of sectors of sparse angle data. Concomitant with these results, 3D SAR imaging of ground reflecting surfaces has shown much promise for synthetic aperture radar processing. A key factor in achieving such 3D images is precise control over the grid (motion) used by the radar sensor. A particular advancement in this research area is the technique referred to as interferometric SAR (IF-SAR). For this case, a unique sampling grid is generated that allows “overlying” of nearly identical 2D range-Doppler images and uses phase differences between these images to estimate the “out-of-plane” height information, from which a 3D image is developed.

In this report, we develop a framework connecting these two techniques, particularly applicable to forming 3D images of target types typically characterized by smaller numbers (≤ 20) of dominant scattering centers, and characterized by deterministic exoatmospheric motion having Euler dynamic spin and precession. For the application considered here, the 3D image is formed using the localized microdynamic changes in look angles to the target characterized by Euler’s 6 Degrees-of-Freedom (6DOF) dynamical equations of motion. This type of motion allows the formation of short-time-interval range-Doppler images at nearly constant look angle K to the time invariant angular momentum vector J . This short-time processing is contrasted with longer-time ISAR imaging of satellites, where changes in look angle to the target are obtained from changes in the long-term trajectory of the satellite.

In essence a SAR interferometric radar measures height by comparing the phase of corresponding range-Doppler image planes, calibrated for sensor motion, to estimate the “projection height” or 3D information contained in the two nearly identical in amplitude data sets. References [5–7] provide a good discussion of the basic principles and associated radar calibration requirements. Various schemes for collecting the SAR data are discussed, each focused on the peculiar hardware calibration requirements inherent in applying these techniques. For the ISAR sensor development presented here, two cases are considered: monostatic (single sensor) and bistatic (two sensors). When applied to a single sensor, these calibration problems are essentially eliminated and replaced by the need for an accurate motion solution and apply to a specific type of target motion. For the bistatic case, a different set of calibration requirements apply, as discussed in subsequent text.

For a single monostatic sensor, the essence of the applicability of these IF-ISAR techniques to Euler-type motion is the observation that, for the case when the spin frequency, f_s , is much greater than the precession frequency, f_p , and if the precession cone angle is not too large, range-Doppler images at roll intervals ϕ and $\phi + 2\pi$ look nearly identical, making the range-Doppler scatterer correlation problem relatively simple. Once individual scattering centers are correlated between images, the phase difference between images can readily be determined and used to augment the basic snapshot imaging equations developed in [1]. (Note: In theory, the phase difference between scattering locations can be used at any point along the dynamical motion. However, the practical problem of tracking and correlating specific scatterers over extended time intervals generally prohibits this.) We show that the utility of the technique degrades gracefully, i.e., when the precession cone angle becomes large, and the increment in aspect $\Delta\theta$ occurring at the roll angles ϕ and $\phi + 2\pi$ is greater than allowed by Nyquist sampling (for which the extracted phase difference between images for some scatterers exceeds 2π , and therefore becomes ambiguous), the standard snapshot equations, without phase, remain valid; yet one still has full advantage of the simpler track correlation problem.

2. EULER MOTION AND SAMPLING CONSIDERATIONS

We assume a target centered coordinate system as illustrated in Figure 1.

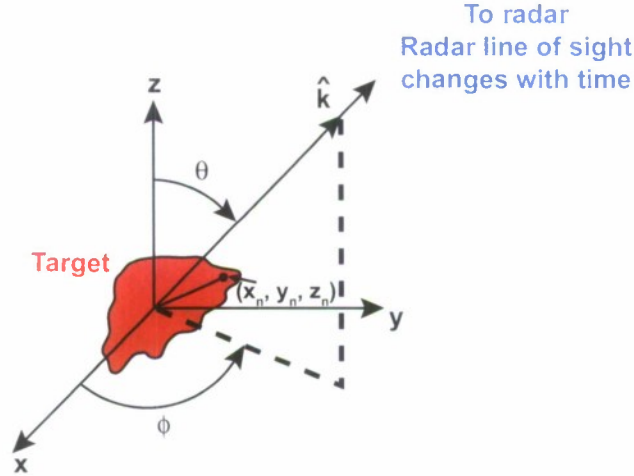


Figure 1. Motion and target scattering reference frames.

Standard spherical coordinates θ, ϕ characterize the look angle to the radar, which is determined by the unit vector \hat{k} , where the notation “^” denotes a unit vector. In general, $\theta(t)$ and $\phi(t)$ are complex functions characterized by Euler’s dynamical equations of motion. The target coordinates (and, hence, the image reference frame) are defined relative to the origin of this system, and an arbitrary scattering point on the target is denoted as (x_n, y_n, z_n) . For a wideband radar operating in the higher frequency bands, the net scattering from the target can be decomposed into scattering from a number of discrete scattering centers, denoted by (x_n, y_n, z_n) , $n=1, \dots, N$. Assume we can isolate a specific scatterer $\underline{r}_n = (x_n, y_n, z_n)$ on the target. In a target-centered coordinate system, this position is fixed, and the look angle to the radar, and its time derivative, are characterized by

$$\hat{k} \cdot \underline{r}_n \equiv R_n \quad (1)$$

$$\dot{\hat{k}} \cdot \underline{r}_n \equiv \dot{R}_n \quad (2)$$

where we define (R_n, \dot{R}_n) to be the range, range rate radar observables corresponding to (x_n, y_n, z_n) , and k and \dot{k} are functions of $\theta, \dot{\theta}, \phi, \dot{\phi}$ given by

$$\hat{k} = \sin \theta \cos \phi \hat{x} + \sin \theta \sin \phi \hat{y} + \cos \theta \hat{z} \quad (3)$$

$$\dot{\hat{k}} = \dot{\theta} \hat{\theta} + \dot{\phi} \sin \theta \hat{\phi} \quad (4)$$

where

$$\begin{aligned} \hat{\theta} &= \cos \theta \cos \phi \hat{x} + \cos \theta \sin \phi \hat{y} - \sin \theta \hat{z} \\ \hat{\phi} &= -\sin \phi \hat{x} + \cos \phi \hat{y} \end{aligned}$$

Eqs. (1) and (2) form a nonlinear set of equations characterizing the behavior of $\theta(t)$ and $\phi(t)$ and each scattering center (x_n, y_n, z_n). We impose physical constraints on the motion $\theta(t)$ and $\phi(t)$ by constraining $\theta(t)$ and $\phi(t)$ to that body motion following from Euler's dynamical equations in a torque-free environment. To this end, we require a closed form transformation, F , of the type

$$F\{\kappa, \theta_p, \phi_p, \psi, f_s, f_p, \alpha_s, \alpha_p, t\} \rightarrow \theta(t) \text{ and } \phi(t) \quad (5)$$

where

κ	=	localized aspect angle from the radar to the target angular momentum vector
θ_p	=	precession cone angle relative to target angular momentum vector
ϕ_p	=	precession rotation angle
ψ	=	spin angle
f_s	=	spin frequency
f_p	=	precession frequency
α_s	=	spin phase
α_p	=	precession phase

Eq. (5) imposes physical constraints on the motion valid for torque-free exoatmospheric-type targets. The closed-form relationship defined by (5) is readily determined using the coordinate transformations developed in [8] and is summarized below.

The aspect angle $\theta(t)$ is dependent on the precession parameters according to

$$\theta(t) = \cos^{-1} \left[\cos \kappa \cos \theta_p + \sin \kappa \sin \theta_p \sin \phi_p \right]. \quad (6)$$

The roll angle $\phi(t)$ is dependent on spin and precession variables according to

$$\phi(t) = +\psi - \tan^{-1} \left(\frac{\cos \kappa \sin \theta_p - \sin \kappa \cos \theta_p \sin \phi_p}{\sin \kappa \cos \phi_p} \right). \quad (7)$$

The closed-form analytic expressions defined by (6) and (7) are extremely useful in understanding the dependence of (θ, ϕ) on any specific type of Euler motion.

A special case of interest occurs for θ_p small. In this case, the expressions $\theta(t)$, $\phi(t)$ reduced to the simpler forms [carrying out the small angle expansions to order (θ_p)]

$$\theta(t) = \kappa - \theta_p \sin \phi_p, \quad (8)$$

$$\phi(t) = 2\pi f_\phi t - \theta_p \cot \kappa \cos \phi_p, \quad (9)$$

where

$$\phi_p = 2\pi f_p t + \alpha_p, \quad (10)$$

and we define the "first order" roll frequency $f_\phi = f_s + f_p \equiv 2\pi/T_\phi$, where T_ϕ is the first order roll period. The roll period, T_ϕ , is in fact most directly inferred from radar observables. Note that T_ϕ as defined above is a first-order approximation to the instantaneous roll frequency $T(t) \equiv 2\pi/\dot{\phi}$.

Figure 2 illustrates the temporal variation of $\theta(t)$, $\phi(t)$ and the corresponding vector $\hat{k}(t)$ for the case where $\theta_p = 2.7^\circ$, $f_s \sim 7 * f_p$, and $T_p = 4$ seconds. Note the helical nature of $\hat{k}(t)$, plotted over the time interval $T_p/2$, characteristic of spinning, precessing motion. We can use the variation of $\hat{k}(t)$ in Figure 2 to contrast the sampling grid that occurs using traditional IF-SAR techniques. This contrast is illustrated in Figure 3.

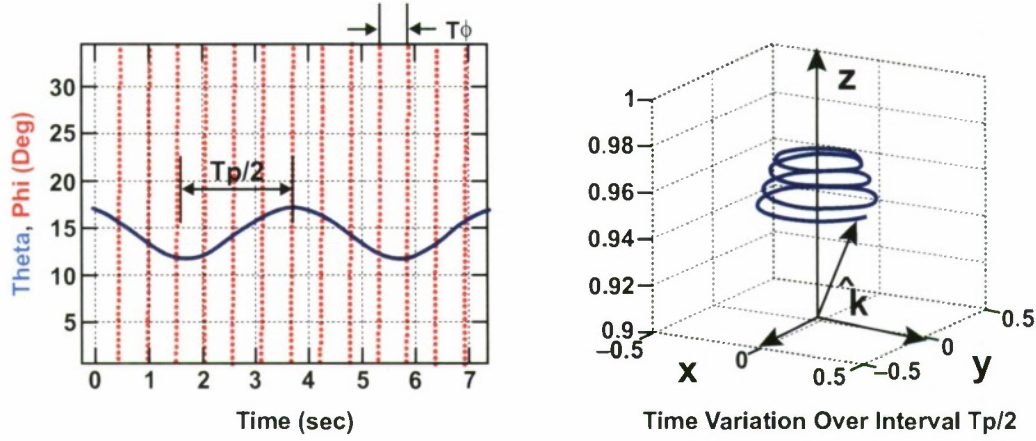


Figure 2. Euler motion (θ , ϕ and \hat{k} vs. time) for small precession and $f_s \gg f_p$

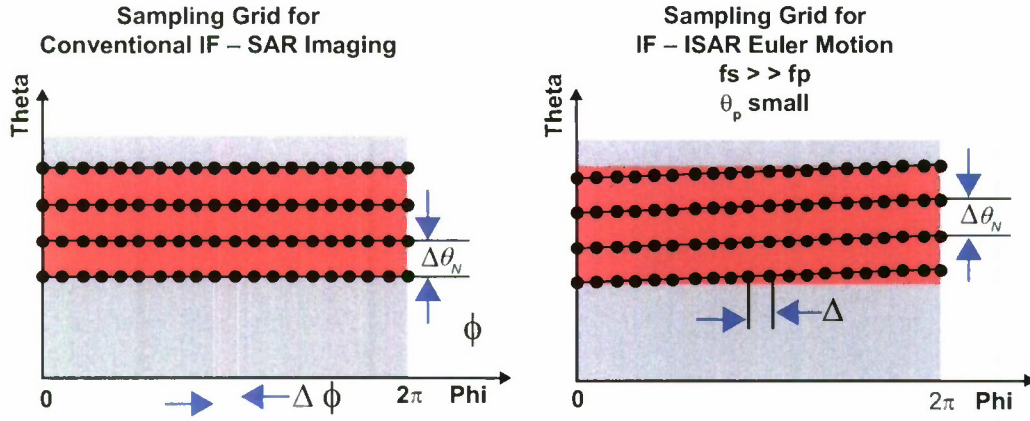


Figure 3. IF-ISAR sampling grids.

Note that for conventional IF-SAR, the aspect θ is constant over the principle $(0, 2\pi)$ ϕ intervals shown, whereas for spinning, precessing motion, $\theta(t)$ is constantly changing over the sampling interval.¹ For either case, extracting an unambiguous phase difference between regions ϕ and $\phi + 2\pi$ requires the sampling interval $\Delta\theta_N$ be less than Nyquist, i.e.,

¹ The sampling grid illustrated for IF-ISAR for spin and precession motion is somewhat simplistic, for illustration purposes. See Figure 10 for a more typical case.

$$\Delta\theta_N < \lambda_0 / (2 * \text{Projected Target Length}), \quad (11)$$

where λ_0 denotes the wavelength at hard center $f = f_0$.

As mentioned earlier, the utility of using 3D snapshot imaging is the ability to generate 3D target images over only a sparse-angle observation space. In Figure 4, we compare several cases illustrating the physical occurrence of sparse-angle sampling compared to the full $4*\pi$ steradian sampling space. The sparseness of spin, precession sampling is clearly evident. For comparison, RCS measurement data collected on a typical radar cross section (RCS) range most clearly correlates to the special cases of “pure tumble” ($\phi = \text{constant}$) and “pure spin” ($\theta = \text{constant}$). The sampling grid associated with phase-enhanced IF-ISAR for the special case $f_s \gg f_p$ considered in this report is also shown for comparison.

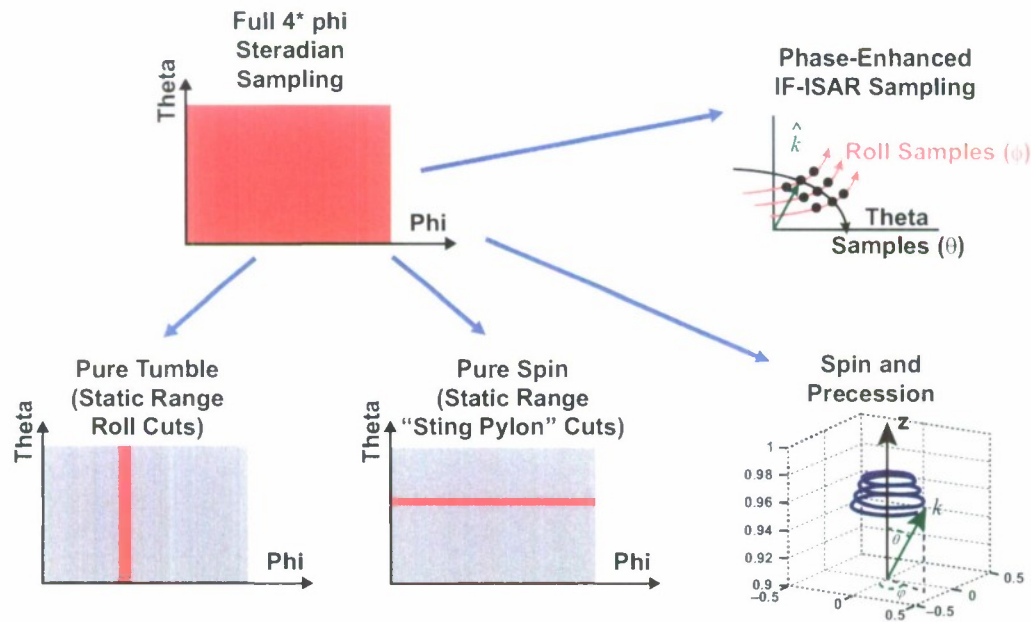


Figure 4. Types of sparse-angle sampling.

Figure 5 contrasts the sampling grid behavior using phase-enhanced snapshot processing vs. conventional snapshot processing. Using conventional snapshot processing, we see that, for $f_s \gg f_p$, the spectral sequence variable \hat{R} is dominated by $\dot{\phi}$ information over a single roll segment, whereas phase-enhanced snapshot processing provides both $\dot{\phi}$ and $\dot{\theta}$ Doppler information by including the θ samples between fixed roll cuts. We show later that this results in considerably greater linear independence of the phase-enhanced snapshot equations vs. conventional snapshot imaging.

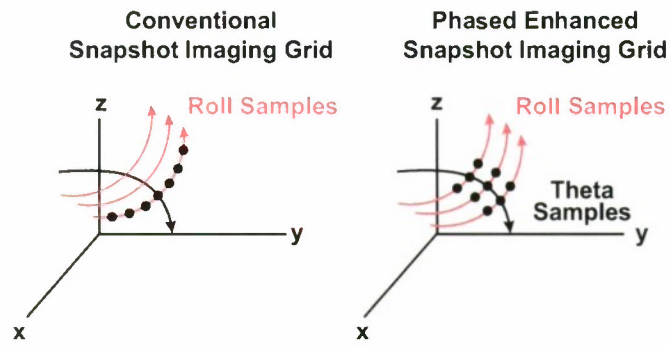


Figure 5. Snapshot sampling: conventional vs. phase-enhanced.

3. DEVELOPMENT (SINGLE MONOSTATIC SENSOR)

Consider the geometry illustrated in Figure 1. Using the Geometrical Theory of Diffraction (GTD) [9], applicable to the high frequency region under consideration, monostatic backscatter from the target can be written in the form

$$E_1^s = \sum_n D_n e^{+j\frac{4\pi}{\lambda} \hat{k}_1 \cdot r_n} \quad (12)$$

where the set $\{r_n\}$, $n=1, \dots, N$ denotes the N dominant scattering centers on the target, each located at (x_n, y_n, z_n) , having complex amplitude D_n , and \hat{k}_1 denotes the radar line-of-sight (LOS) unit vector. Typically, D_n is a relatively slow varying function of (f, θ, ϕ) and characterizes the GTD diffraction coefficient of the n th scattering center. It is essentially constant over the data-block under consideration when using sequential block processing. Denote $\hat{k} = \hat{k}_1$ at time $t = t_1$, and $\hat{k} = \hat{k}_2$ at $t = t_2$ where $t_2 > t_1$. Now assume that at the later time, $t = t_2$, the scattered field is sampled in a direction \hat{k}_2 . Furthermore, if we assume \hat{k}_2 is "close" to \hat{k}_1 , then we can express

$$\hat{k}_2 = \hat{k}_1 + \underline{\Delta k} \quad (13)$$

Using (13) in the general expression for the scattered field, the scattered field E_2^s at $t = t_2$ can be expressed in the form

$$E_2^s = \sum [D_n^1 e^{+j\frac{4\pi}{\lambda} (\Delta k \cdot r_n)}] e^{+j\frac{4\pi}{\lambda} \hat{k}_1 \cdot r_n} \quad (14)$$

Now assume that, since \hat{k}_2 is assumed close to \hat{k}_1 , the 2D range-Doppler images extracted from each 2D data block centered at times $t = t_1$ and $t = t_2$, respectively, are nearly identical, so that the individual scattering centers in each image can readily be identified and correlated. By extracting the phase of each scattering center from the range-Doppler image, Eqs. (12) and (14) can be compared to obtain

$$Phase(I_{2n}) - Phase(I_{1n}) = Phase(D_n^1) - Phase(D_n) + \frac{4\pi}{\lambda} (\hat{k}_2 - \hat{k}_1) \cdot r_n \quad (15)$$

where I_n denotes the complex amplitude of the image pixel of the n th scattering center. If $\vec{k}_2 - \vec{k}_1$ is close to Nyquist sampling, then $D_n^1 \approx D_n$ so that (15) can be written in the form

$$\frac{4\pi}{\lambda}(\hat{k}_2 - \hat{k}_1) \bullet r_n = \Delta_n(Phase), \quad (16)$$

where we define:

$$\Delta_n(Phase) = Phase(I_{2n}) - Phase(I_{1n}) \quad (17)$$

where I_{1n} and I_{2n} represent the complex amplitude defined over each respective range-Doppler image plane.

Eq. (16) will be used in the next section to augment the standard set of 3D snapshot imaging equations.

It should be noted that Eqs. (15–17) as derived are equivalent to the standard characterization of IF-SAR processing. They are repeated in this manuscript only to emphasize their coupling to the 3D snapshot imaging equations.

4. THE GENERALIZED “PHASE-ENHANCED” SNAPSHOT IMAGING FRAMEWORK

In this section, we first review the methodology of generating a 3D snapshot image described in [1] and then augment this basic equation set with the phase-enhanced equations developed in Section 3.

Consider first the process of sequentially extracting the range, range-rate information from a 2D radar data block. Typically, a wideband radar transmits a sequence of pulses, each of which interrogates the target over a given frequency band $f_0 - BW/2$ to $f_0 + BW/2$, where f_0 is the RF carrier frequency and BW the bandwidth of the radar. Each pulse in the time sequence is spaced at time interval Δt , where the PRF of the radar is given by $PRF = 1/\Delta t$. Denote the signal received (after matched filtering) by the radar on each pulse as $e_q(t)$, where the index “q” denotes the pulse label. Denote the unweighted Fourier transform of $e_q(t)$ as $E_q(\omega)$, where $\omega = 2\pi f$ is a continuous frequency variable and f ranges over the bandwidth ($-BW/2$ to $BW/2$). Assume f is sampled at frequency intervals $f = k \Delta f$. Then the data matrix $E_q(k) \equiv E(k, q)$ represents a 2D (frequency, pulse) representation of the field scattered by the target. A conventional linear image could then be obtained using a 2D Fourier transform on $E(k, q)$. For our purposes, it is more useful to consider the raw data block $E(k, q)$ and optimally extract target information from this block using recently developed 2D spectral estimation techniques [10,11,12]. As time “marches on,” sequences of data blocks each incremented by Δt can be processed. We refer to this as sequential block processing. The overall process is illustrated in Figure 6 using simulated data from a cone-like target having extended fins (see Figure 8).

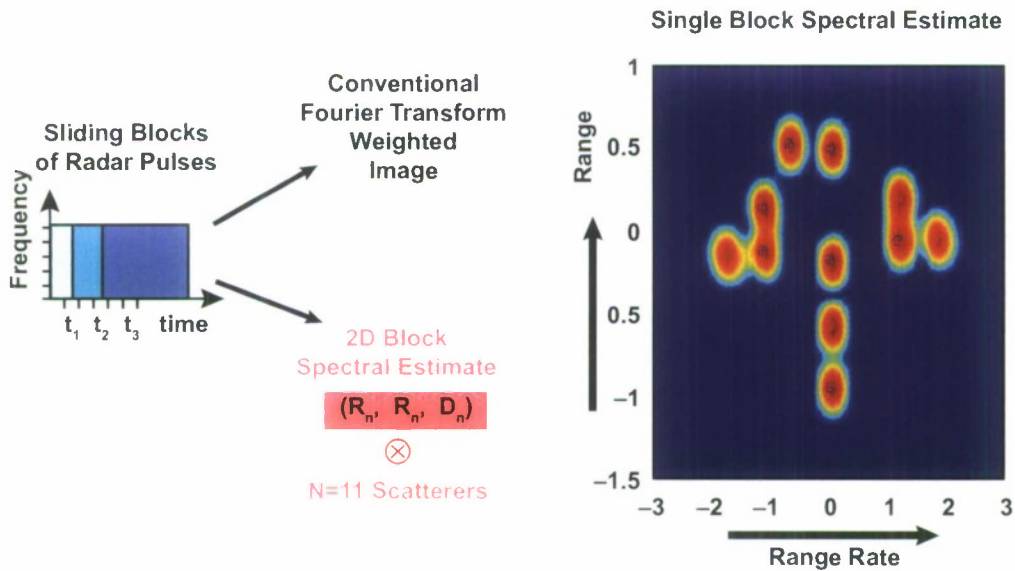


Figure 6. Component extraction using block processing vs. conventional Fourier image.

Two-dimensional blocks of radar data are processed sequentially to develop a range, range-rate spectral sequence $\{R_n, \dot{R}_n\}_{q,t=t_1,\dots,t_q}$ as illustrated in Figure 6. Typically, an R, \dot{R} correlator/smoother is implemented to track these poles in R, \dot{R} space by sequentially processing a block of pulses through the measurement data set. Eqs. (1, 2) are then applied sequentially to a number of snapshots to develop an image of the scattering points (x_n, y_n, z_n) . To illustrate this process mathematically, express the transformation defined by Eqs. (1) and (2) in matrix form:

$$\underline{T}_{q_1} \cdot \begin{bmatrix} x_n \\ y_n \\ z_n \end{bmatrix} = \begin{bmatrix} R_n \\ \dot{R}_n \end{bmatrix}_{q_1}, \quad (18)$$

where \underline{T} is a 2×3 transformation matrix given by

$$\underline{T} = \begin{bmatrix} \hat{k} \\ \dot{\hat{k}} \end{bmatrix},$$

where \hat{k} and $\dot{\hat{k}}$ are expressed as row vectors and (18) defines the mapping at $t = tq_1$. We can accumulate these equations for two snapshots at tq_1 and tq_2 in the form

$$\begin{bmatrix} \underline{T}_{q_1} \\ \underline{T}_{q_2} \end{bmatrix} \cdot \begin{bmatrix} x_n \\ y_n \\ z_n \end{bmatrix} = \begin{bmatrix} \begin{pmatrix} R_n \\ \dot{R}_n \end{pmatrix}_{q_1} \\ \begin{pmatrix} R_n \\ \dot{R}_n \end{pmatrix}_{q_2} \end{bmatrix}. \quad (19)$$

As additional snapshots are obtained, these equations are added to (19), which is then solved in a least squares sense for the scattering coordinates (x_n, y_n, z_n) .

The rank of \underline{T} and hence the solutions for (x_n, y_n, z_n) clearly depend on numerous variables. Some of these are the observed motion of the target, the number of snapshots, the time spacing between snapshots, and the signal-to-noise ratio present in the data. A detailed analysis of these variables relative to their effect on the resultant image has not been carried out. In applications to actual field data not presented here, we demonstrated good results by implementing some smoothing of the range, range-rate data before applying (19).

Consider now augmenting the basic snapshot equation set with using the phase-extracted information defined by Eq. (16). Note that by examining Figure 5, \dot{R} information is extracted from data along the direction of motion. For example, for spin-only, at constant aspect θ_0 , $\dot{\theta} = \dot{\theta}$, and using Eq. (4)

$$\dot{\phi} \sin \theta_0 \hat{\phi} \bullet \underline{r}_n = \dot{R}_n,$$

i.e., \dot{R} is characterized solely by $\dot{\phi}$ for this case. This corresponds to the localized spin-dominated motion illustrated in Figure 5 for conventional snapshot processing when $f_s \gg f_p$.

The sampling grid for phased-enhanced snapshot imaging illustrated in Figure 5 provides additional independent information by augmenting Eq. (18) with data blocks associated with changes in θ i.e., $\theta = \theta_0 + \Delta\theta$ when $\phi = \phi + 2\pi$. Eq. (18) is then augmented by the additional Eq. (16) developed in Section 3:

$$\frac{4\pi}{\lambda} (\hat{k}_2 - \hat{k}_1) \bullet \underline{r}_n = \Delta_n \text{ (phase)}, \quad (20)$$

where the subscript "2" is defined to be at sample time corresponding to roll angle $\phi + 2\pi$ and Δ_n (phase) is the phase difference for the scatter at (x_n, y_n, z_n) at each respective roll angle. Clearly for Δ (phase) to be nonambiguous, the change $\Delta\theta$ in aspect cannot exceed Nyquist.

Note, in principle, augmenting Eq. (18) with (20) provides three independent equations to directly solve for the three unknowns (x_n, y_n, z_n) . That Eq. (20) provides independent information can be readily seen by evaluating $(\hat{k}_2 - \hat{k}_1)$ directly assuming $\theta = \theta_0 + \Delta\theta$ at $\phi = \phi + 2\pi$. It can readily be shown that

$$\frac{4\pi}{\lambda} (\hat{k}_2 - \hat{k}_1) \bullet \underline{r}_n = \frac{4\pi}{\lambda} \Delta\theta \hat{\theta} \bullet \underline{r}_n. \quad (21)$$

The three resulting equations are approximately given by

$$\sin \theta \cos \phi x_n + \sin \theta \sin \phi y_n + \cos \theta z_n = R_n \quad (22)$$

$$\dot{\phi} \sin \theta \hat{\phi} \bullet \underline{r}_n = \dot{R}_n \quad (23)$$

$$\frac{4\pi}{\lambda} \Delta\theta \hat{\theta} \bullet \underline{r}_n = \Delta_n (\text{phase}) . \quad (24)$$

Eqs. (22), (23), and (24) have an interesting graphical interpretation which illustrates the basic orthogonality (and consequent linear independence) of the equation set, as illustrated. The localized orthogonal system is illustrated in Figure 7. Recall that \hat{k} is a unit vector in the direction of the radar LOS. Since \hat{k} is perpendicular to $\hat{\theta}, \hat{\phi}$, the three unit vectors $(\hat{k}, \hat{\phi}, \hat{\theta})$ form a local (i.e., a function of θ, ϕ) orthogonal set of unit vectors, defining a local 3D axis set. Eqs. (22–24) then can be written in the form

$$\begin{aligned} \hat{k} \bullet \underline{r}_n &= R_n \\ \hat{\phi} \bullet \underline{r}_n &= \dot{R}_n / (\dot{\phi} \sin \theta) \\ \hat{\theta} \bullet \underline{r}_n &= \frac{\lambda}{4\pi} \bullet \Delta_n (\text{phase}) / \Delta\theta , \end{aligned} \quad (25)$$

which clearly delineate the projections of the scattering center location vector \underline{r}_n onto the axes of this localized orthogonal frame.

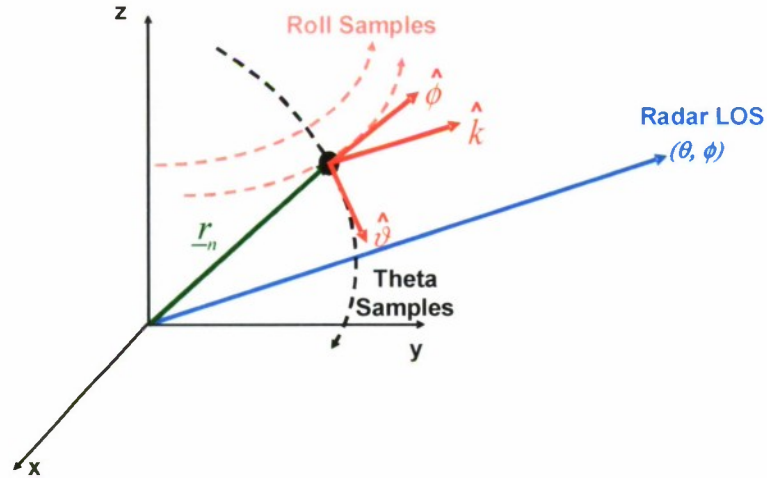


Figure 7. Localized orthogonal coordinate system for 3D phase-enhanced precessing.

Although Eq. (25) is directly invertible to solve for (x_n, y_n, z_n) using a single “snapshot,” it is still useful to use a cumulative approach that provides smoothing in the presence of noisy data. To this end we rewrite Eq. (25) in the form

$$\underline{T}_{=q} \bullet \underline{R}_n = \begin{bmatrix} R_n \\ \dot{R}_n \\ \Delta(n) \end{bmatrix}, \quad (26)$$

where now $\underline{T}_{=}$ is the 3×3 motion matrix defined by

$$\underline{T}_{=} \equiv \begin{bmatrix} \hat{k} \\ \hat{\phi} \sin \theta \hat{\phi} \\ \frac{4\pi}{\lambda} \Delta \theta \hat{\theta} \end{bmatrix}. \quad (27)$$

We then accumulate observation samples in a manner analogous to Eq. (19).

$$\begin{bmatrix} \underline{T}_{=q_1} \\ \underline{T}_{=q_2} \\ \vdots \end{bmatrix} \cdot \begin{pmatrix} x_n \\ y_n \\ z_n \end{pmatrix} = \begin{bmatrix} \begin{pmatrix} R_n \\ \dot{R}_n \\ \Delta(n) \end{pmatrix}_{q_1} \\ \begin{pmatrix} R_n \\ \dot{R}_n \\ \Delta(n) \end{pmatrix}_{q_2} \end{bmatrix} \quad (28)$$

Solutions to Eq. (28) in the last-squares sense then provide a more robust estimate of each scattering location (x_n, y_n, z_n) .

This page intentionally left blank.

5. SIMULATION

We now develop an example showing the utility and methodology used to implement the enhanced snapshot imaging equations. Consider the cone-like target geometry illustrated in Figure 8.

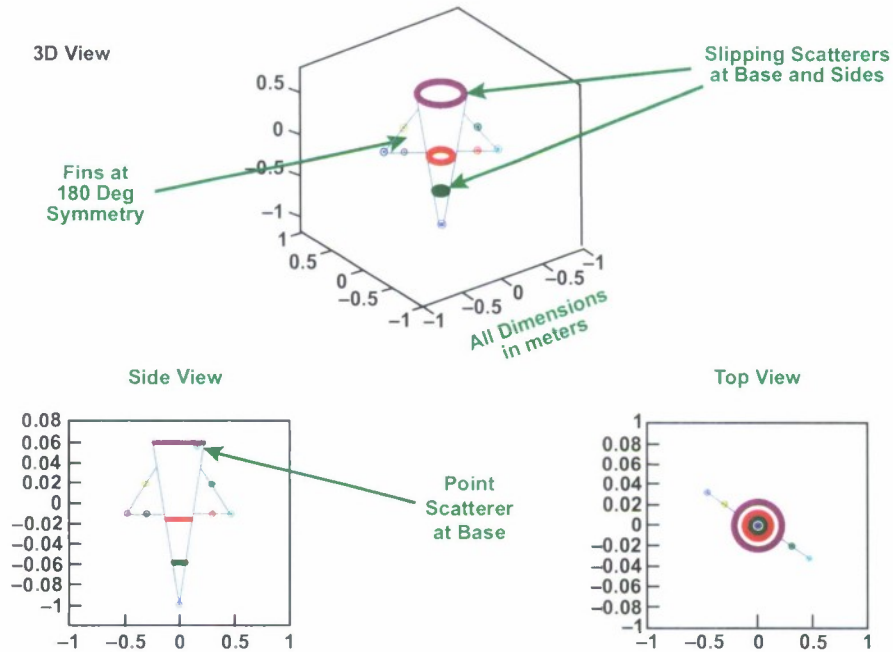


Figure 8. RV simulation geometry.

X-band wideband scattering data having 1 GHz bandwidth were simulated using an 11-point, point-scatter model (without shadowing), with each scatterer having unity amplitude and (fixed) random phase. For illustrative purposes, the scattering phenomena includes both slipping scatterers on the base and sides of the cone, and point scatterers on the fins, as well as a point scatterer located just below the base and on the "nose." Slipping scatterers are particularly interesting because they exhibit no Doppler with changes in roll angle (e.g., azimuthally symmetric slots, ridges, and edges). The assumed motion parameters and associated $\theta(t)$, $\phi(t)$ motion used to generate the data sequence $E^s\{f_k, t_q\}$, where E^s denotes the scattered field, are tabulated in Figure 9 along with plots of the associated motion $\theta(t)$, $\phi(t)$. Note the rapid change in $\phi(t)$ (shown in "dotted red" and clipped over the plot region) vs. the slow change in $\theta(t)$ characterized by $f_s \gg f_p$. Of particular interest for this target is the Nyquist sampling limit $\Delta\theta_N$ defined by Eq. (11). For target length ~ 1.5 m at near "nose-on" aspect, $\Delta\theta_N \approx 0.75$ deg.

A typical range-Doppler image used to extract the sequence $\{R_n, \dot{R}_n\}_q$ is also shown in Figure 9.

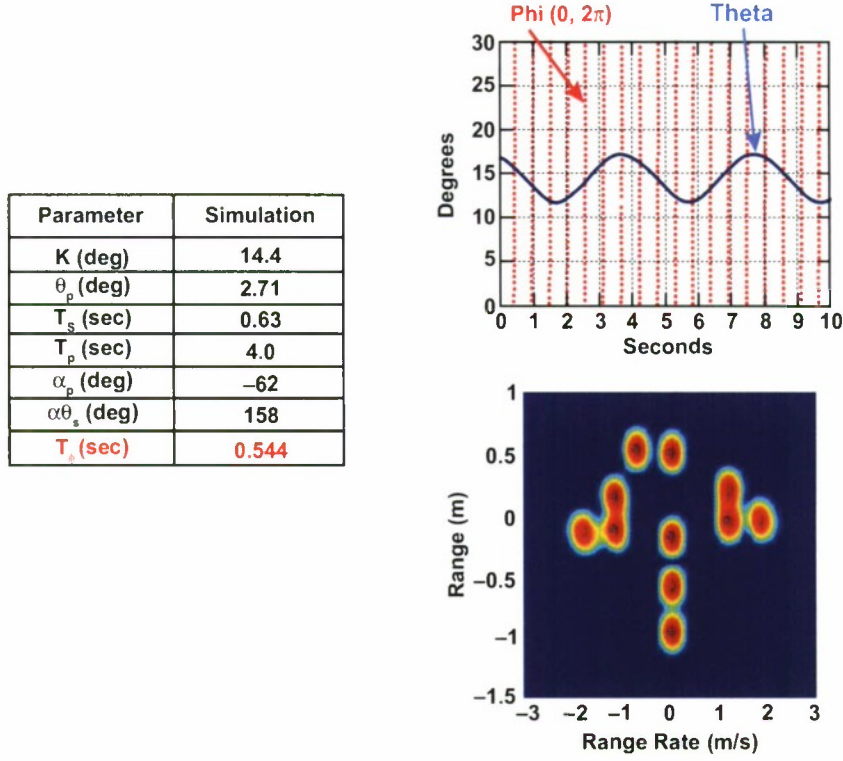


Figure 9. Simulation motion parameters $\theta(t)$, $\phi(t)$ and typical range-Doppler image.

Figure 10 illustrates a different characterization of the variation of $[\theta(t), \phi(t)]$ for the assumed motion over several roll eyeles, where we plot $\theta(t)$ vs. $\phi(t)$ parametrically vs. time. The “arrows” on the blue trace illustrate the direction change vs. time. The “phi-cuts” illustrated represent typical theta values at $\phi = \phi + 2*n*\pi$ jumps. We clearly see that for the value of θ_p considered, for some cases, the change $\Delta\theta$ between $\Delta\phi = 2\pi$ jumps is greater than Nyquist. However, in the region $\dot{\theta} \approx 0$, i.e., along the upper portion of the trajectory, the change delta theta is below Nyquist for the assumed $\theta_p = 2.71^\circ$. Thus, for example, the processing region indicated on the figure is well suited to apply phase-enhanced 3D imaging. For other regions, conventional snapshot imaging techniques would be applicable.

By extending the above discussion, and using the small precession expressions for $\dot{\theta}(t), \phi(t)$ defined by Eq. (8), one can readily show that when operating about the region $\dot{\theta} \approx 0$, the precession angle θ_p is restricted by the more general relationship.

$$\theta_p < \frac{2}{\pi^2} \cdot \left(\frac{T_p}{T_\phi}\right)^2 \Delta\theta_{\text{Nyq}}. \quad (29)$$

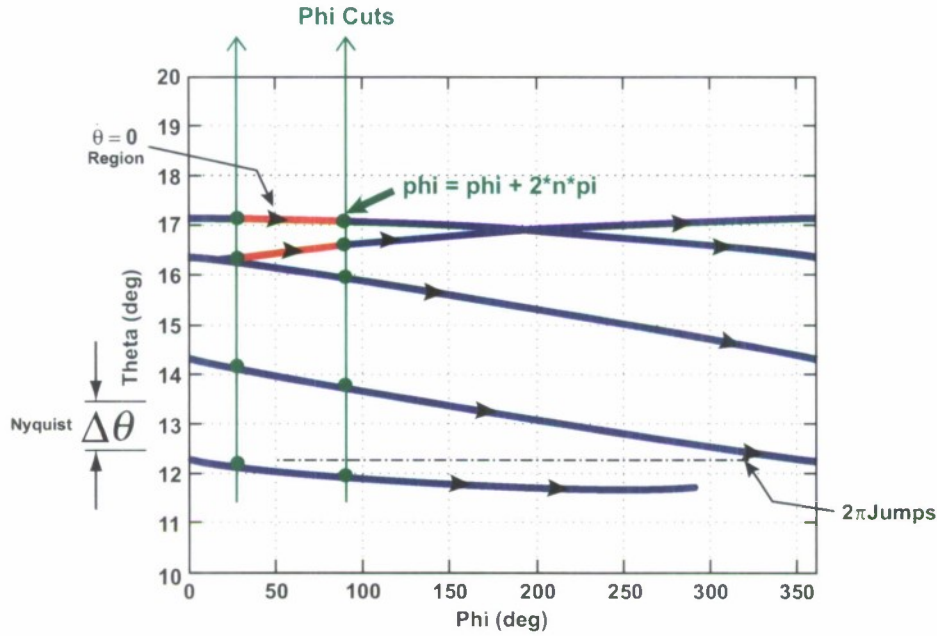


Figure 10. $\theta(t)$ vs. $\phi(t)$ illustrated parametrically in time.

The above discussion leads to a methodology one might apply for cases when the precession angle θ_p is considerably larger than Nyquist:

1. Isolate regions about $\dot{\theta} \approx 0$.
2. Choose a value $\phi = \phi_0$. Search on t_q for $\phi = \phi + 2\pi$ according to $t_q = \text{find} [\phi(t_q) = \phi_0 + 2\pi]$.
3. Process the associated sequential pairs of images for the times t_0, t_q according to Eq. (28).
4. Sequentially accumulate estimates, by sliding t_0 in steps Δt , keeping within the bounds of the Nyquist sampling criteria.

The above methodology applied to the simulation example considered leads to a processing interval indicated as the red portion of the $[\theta, \phi]$ grid illustrated in Figure 10.

In Figure 11, we illustrate a magnification of the $[\theta, \phi]$ sampling region corresponding to the red portion of Figure 10, indicating the θ, ϕ values associated with t_0 ($\phi = \phi$) and t_q ($\phi = \phi + 2\pi$). Clearly, the change $\Delta\theta$ over this region is less than Nyquist, which for the aspect angle considered corresponds to approximately 0.75° . Also shown in the Figure are the (R, \dot{R}) values extracted from the range-Doppler images at time $t = t_0$ as t_0 progresses over the indicated region.

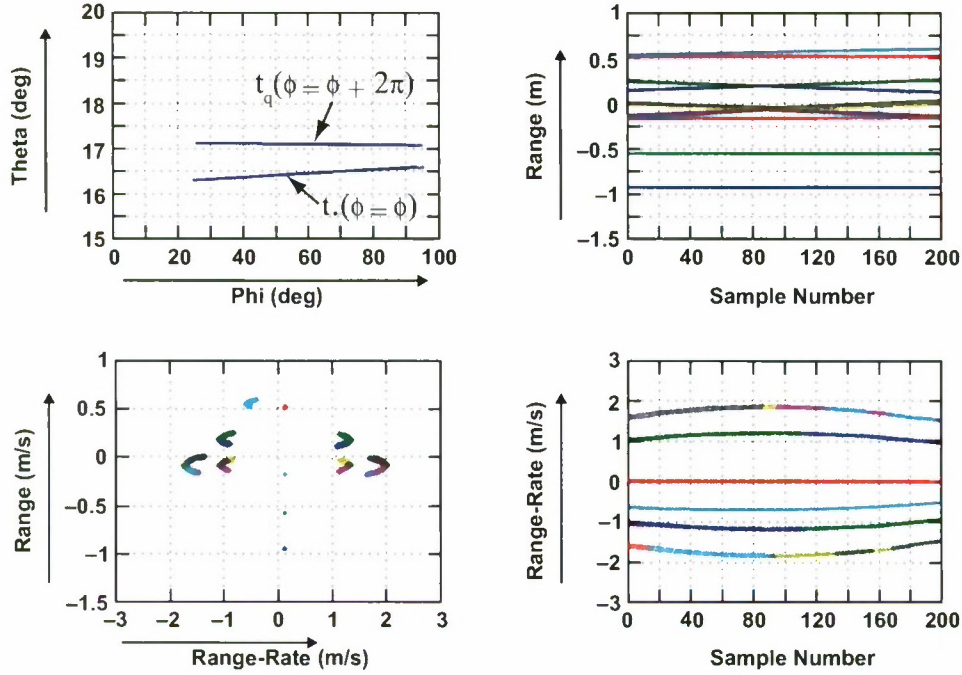


Figure 11. Image grid and extracted poles.

In Figure 12, we illustrate the composite of these (R, \dot{R}) pairs for each of the sliding intervals $[t_0]$ and $[t_q]$. Note the close correspondence of the range-Doppler images as each scatterer appears only slightly displaced due to the change in aspect $\Delta\theta$. Note also from Figure 11 that, in fact, $\Delta\theta$ changes with time increment as t_0 is incremented over the processing interval.

Figure 13 illustrates the 3D image obtained when applying the phase-enhanced snapshot equations to the $\{R_n, \dot{R}_n, \Delta(\text{phase})_n\}$ sequence. Note that because the technique provides an independent estimate of the actual 3D location of each scatterer as contrasted to a conventional range-Doppler image where the location of an image peak must be estimated, the 3D “images” presented here are actually estimates of the 3D locations of the individual scattering centers. The amplitudes and frequency characteristics of each scatterer are extracted separately, as discussed in [1].

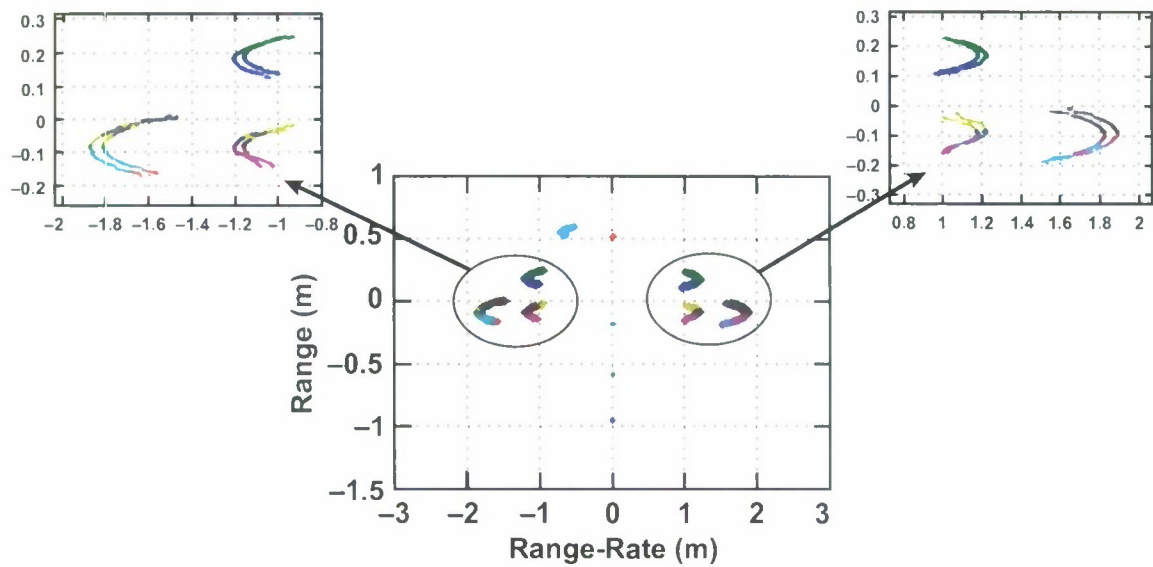


Figure 12. Range-Doppler pairs ($t = t_0$ vs. $t = t_q$).

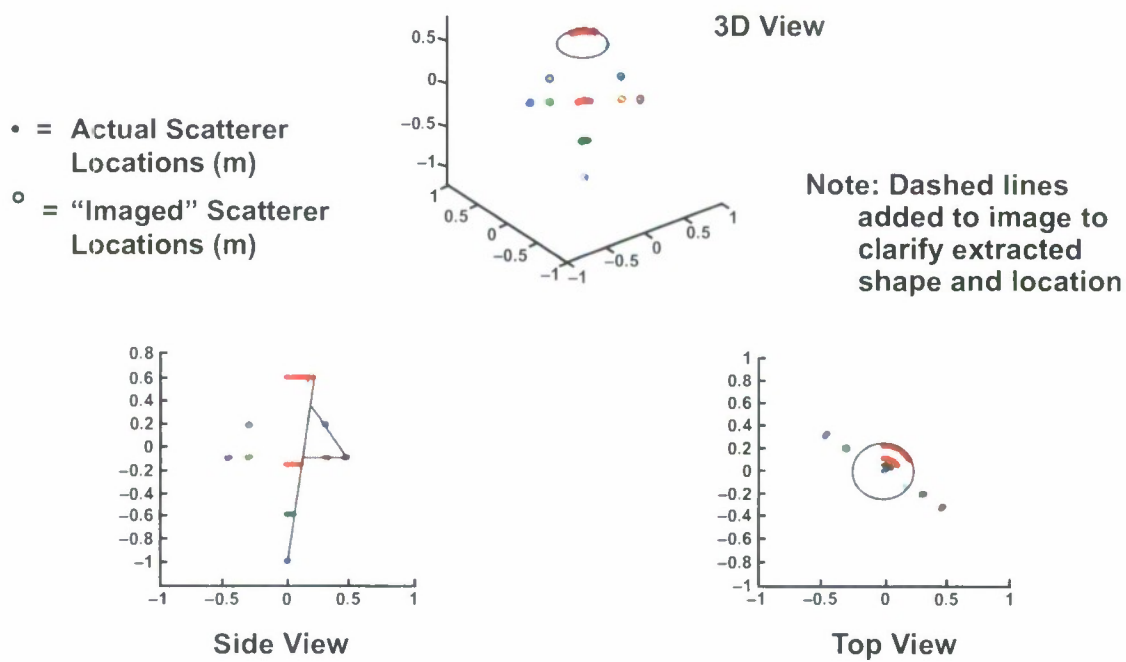


Figure 13. Phase-enhanced 3D snapshot image.

Two facts are immediately obvious upon examination of the results of Figure 13.

The phase-augmented snapshot equations correctly image the slipping scatterers.

The slipping scatterers are imaged on the cone only over the observation interval—in this case the roll angle ϕ given by $28^\circ \leq \phi \leq 92^\circ$.

By comparison, Figure 14 illustrates a 3D target image using conventional snapshot imaging (i.e., no phase) over a region where $\Delta\theta > \text{Nyquist}$ when $\phi = \phi + 2\pi$ as indicated on the insert. Over this observation region, the precession causes too large a change in θ over one roll cycle so that the extracted phase is ambiguous, and conventional snapshot image techniques must be used. Note, however, that in this case the slipping scatterers are not properly located and project to the z-axis.

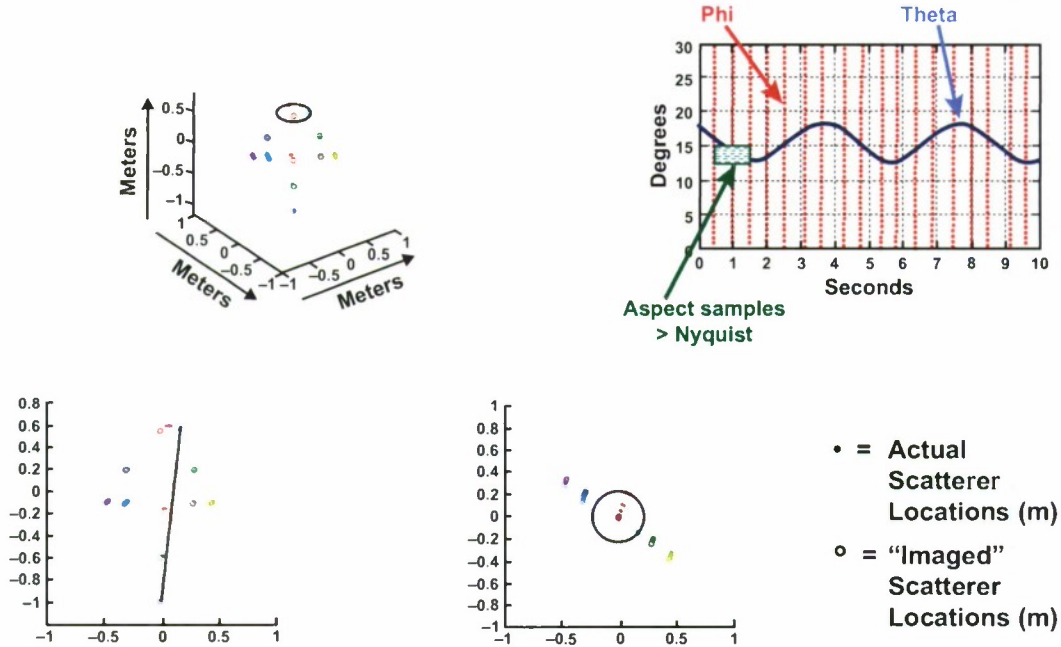


Figure 14. Conventional snapshot imaging (aspect sample $>$ Nyquist).

6. APPLICATION TO BISTATICS

Upon close examination of the development in Section 3.0, it becomes evident that the phase information contained in interrogating the target from directions \hat{k}_1 and \hat{k}_2 need not be obtained sequentially. The general development, with limited modification, holds if the backscatter is obtained from two sensors simultaneously, using either monostatic, bistatic, or multistatic data. However, for the case of more than a single sensor, the issue of coherence, or phase adjustments to the data, must be addressed. We now develop the modifications required for the bistatic case for two sensors labeled "1" and "2". For convenience, we assume sensor 1 operates monostatically, and sensor 2 receives the bistatic data scattered from the incident field of sensor 1.

The backscattered field in the direction of sensor 1 (direction vector \hat{k}_1) is characterized by Eq. (12), except now we must add an arbitrary one-way propagation delay, denoted as τ_1 . For this case

$$E_1^s \sim e^{-j\omega(2\tau_1)} \sum_n D_n e^{+j\frac{4\pi}{\lambda}(\hat{k}_1 \cdot \underline{r}_n)}. \quad (30)$$

In a similar manner, the bistatic field in the direction \hat{k}_2 is given by

$$E_2^s \sim e^{-j\omega(\tau_1+\tau_2)} \sum D_n^1 e^{+j\frac{2\pi}{\lambda}(\hat{k}_1 + \hat{k}_2) \cdot \underline{r}_n}, \quad (31)$$

where again, we assume for \hat{k}_1 close to \hat{k}_2 , $D_n^1 \approx D_n$. Expressing $\hat{k}_2 = \hat{k}_1 + \underline{\Delta k}$, Eq. (27) can be written in the form

$$E_2^s \sim e^{-j\omega(2\tau_1)} \sum_n [D_n^1 e^{+j\frac{2\pi\Delta R}{\lambda}} e^{+j\frac{2\pi}{\lambda}\underline{\Delta k} \cdot \underline{r}_n}] e^{+j\frac{4\pi}{\lambda}\hat{k}_1 \cdot \underline{r}_n} \underline{\hat{R}}_n. \quad (32)$$

Comparing (30) and (31), after extracting the differences in image phase for the nth scatterer, we obtain the modified version of Eq. (20):

$$\Delta_n \text{ (phase)} = \frac{2\pi}{\lambda}(\Delta R) + \frac{2\pi}{\lambda} \underline{\Delta k} \cdot \underline{r}_n, \quad (33)$$

where we have defined the coherence parameter ΔR :

$$\Delta R = c (\tau_2 - \tau_1), \quad (34)$$

and $c = 3 \times 10^8$ m/s. Note, for the bistatic case, the occurrence of the phase factor $(2\pi/\lambda)$ vs. $(4\pi/\lambda)$ in Eq. (33).

Clearly, when using Eq. (32) to augment the snapshot equations, ΔR must be estimated. One can then either correct the data accordingly, or use ΔR in Eq. (33) directly. Techniques for estimating ΔR are described elsewhere [13].

The separation required between \hat{k}_1 and \hat{k}_2 to affect less than Nyquist sampling is directly dependent on the range and projected length of the target. Some typical baseline values, normalized to the Nyquist sampling interval $\Delta\theta_N$, are illustrated in Figure 15.

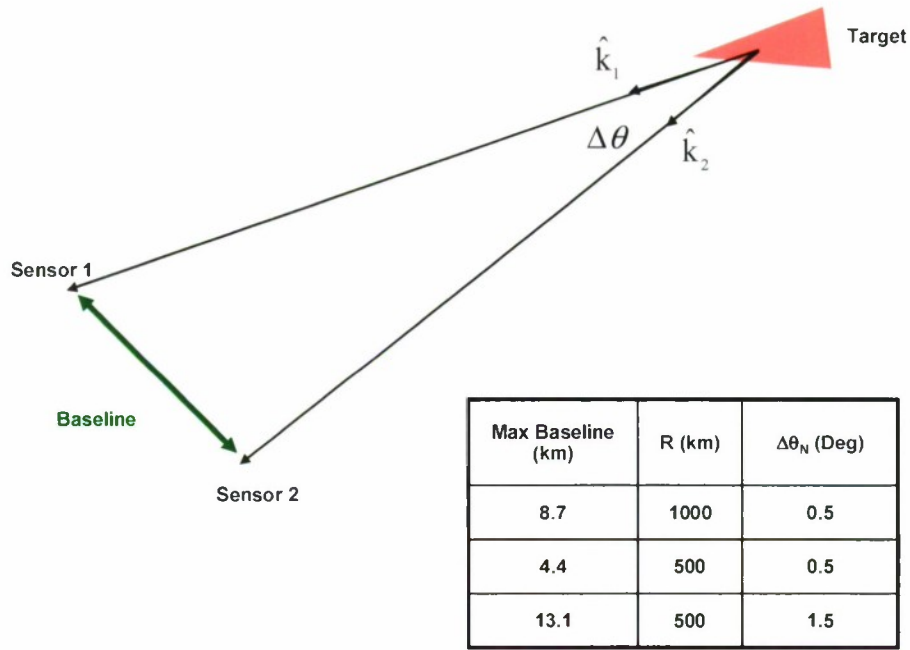


Figure 15. Maximum baseline for bistatic collections.

7. SUMMARY

Three-dimensional interferometric SAR imaging of ground reflecting surfaces has shown much promise for synthetic aperture radar processing. A key factor in achieving such 3D images is precise control over the sampling grid (motion) used by the radar sensor. This report develops a framework based on 3D snapshot imaging of sparse angle sectors of ISAR data, extending these results to 3D interferometric ISAR imaging of targets having deterministic, torque-free exoatmospheric motion characterized by spin and precession.

Essential to the application of these techniques to Euler-type dynamical motion is the existence of a sparse-angle sampling grid over which the phase information extracted from range-Doppler images can be properly utilized. We compare several types of sparse-angle sampling grids to that generated from Euler-type motion and develop an ISAR-based approach to extracting the required phase information.

The framework presented here is an extension of the "3D Snapshot Imaging" technique developed in [1]. A new set of independent snapshot equations are developed, from which image points on the target can be extracted. Because the differential phase extracted between suitable range-Doppler images is required to be nonambiguous, the applicability of the generalized technique requires the precession angle θ_p be relatively small [see Eq. (28)]. However, the noncoherent snapshot image equations remain valid beyond this precession limit, and the unique sampling grid developed is still very useful for 3D imaging of the noncoherent snapshot equation set. Techniques for removing this constraint by resolving the phase ambiguities for $\Delta\theta > \Delta\theta_N$ are under investigation.

A simple simulation is developed illustrating the application of the technique, and extensions to bistatics are developed. Applications of this technique to field data, not presented in this report, have demonstrated good results.

This page intentionally left blank.

REFERENCES

- [1] J.T. Mayhan, M.L. Burrows, K.M. Cuomo, and J.E. Piou, "High Resolution 3D 'Snapshot' ISAR Imaging and Feature Extraction," *IEEE Transactions AES*, (2001).
- [2] D.A. Ausherman, A. Kozma, J.L. Walker, H.M. Jones, and E.S. Poggio, "Developments in Radar Imaging," *IEEE Transactions on Aerospace and Electronic Systems*, **AES-20** (1984), 363–400.
- [3] M.A. Stuff, "Three-Dimensional Analysis of Moving Target Radar Signals: Methods and Implications for ATR and Feature Aided Tracking," *Proceedings of SPIE*, **3721** (1999), 485–496.
- [4] S.J. Hershkowitz, "Use of the Complex Image to Recognize and Trace Multipath Returns in Turntable Data," *Proceedings of 20th AMTA Symposium* (1998), 402–407.
- [5] R.J. Sullivan, "Radar Foundations for Imaging and Advanced Concepts," SciTech Publishing (2000), 224–225.
- [6] B.D. Rigling, and R.L. Moses, "Three Dimensional Surface Reconstruction from Multistatic SAR Images," *IEEE Transactions on Image Processing* (2003).
- [7] W.G. Carrara, et al., "Spotlight Synthetic Aperture Radar," Artech House (1995), 369–374.
- [8] R. A. Becker, Introduction to Theoretical Mechanics, McGraw Hill, (1954), Chap. 12, Sec. 12–13.
- [9] J.B. Keller, "Backscattering From a Finite Conc," *IEEE Transactions on Antennas and Propagation* (1960), 175–182.
- [10] F. Vanpoucke, M. Moonen, and Y. Berthoumicu, "An Efficient Subspace Algorithm for 2D Harmonic Retrieval," *Proceedings of ICASSP*, **4** (1994), 461–464.
- [11] M.L. Burrows, "Two-Dimensional ESPRIT with Tracking for Radar Imaging and Feature Extraction," *IEEE Transactions on Antennas and Propagation*, vol. AP-52, No. 2 (2004), 524–532.
- [12] S.L. Borison, S. Bowling and K.M. Cuomo, "Superresolution Methods for Wideband Radar," *LL Journal*, **5**, 3 (1992) 441–461.
- [13] K.M. Cuomo, J.E. Piou, and J.T. Mayhan, "Ultrawideband Coherent Processing," *IEEE Transactions on Antennas and Propagation*, **47** (1999), 1094–1107.

This page intentionally left blank.

REPORT DOCUMENTATION PAGE				Form Approved OMB No. 0704-0188	
Public reporting burden for this collection of information is estimated to average 1 hour per response, including the time for reviewing instructions, searching existing data sources, gathering and maintaining the data needed, and completing and reviewing this collection of information. Send comments regarding this burden estimate or any other aspect of this collection of information, including suggestions for reducing this burden to Department of Defense, Washington Headquarters Services, Directorate for Information Operations and Reports (0704-0188), 1215 Jefferson Davis Highway, Suite 1204, Arlington, VA 22202-4302. Respondents should be aware that notwithstanding any other provision of law, no person shall be subject to any penalty for failing to comply with a collection of information if it does not display a currently valid OMB control number. PLEASE DO NOT RETURN YOUR FORM TO THE ABOVE ADDRESS.					
1. REPORT DATE 28 December 2009		2. REPORT TYPE Technical Report		3. DATES COVERED (From - To)	
4. TITLE AND SUBTITLE "Phase-Enhanced" 3D Snapshot ISR Imaging and Interferometric SAR				5a. CONTRACT NUMBER FA8721-05-C-0002	
				5b. GRANT NUMBER	
				5c. PROGRAM ELEMENT NUMBER	
6. AUTHOR(S) Joseph T. Mayhan				5d. PROJECT NUMBER 1057	
				5e. TASK NUMBER 3	
				5f. WORK UNIT NUMBER	
7. PERFORMING ORGANIZATION NAME(S) AND ADDRESS(ES) MIT Lincoln Laboratory 244 Wood Street Lexington, MA 02420-9108				8. PERFORMING ORGANIZATION REPORT NUMBER TR-1135	
9. SPONSORING / MONITORING AGENCY NAME(S) AND ADDRESS(ES) Missile Defense Agency/DV 7100 Defense Pentagon Washington, DC 20301-7100				10. SPONSOR/MONITOR'S ACRONYM(S)	
				11. SPONSOR/MONITOR'S REPORT NUMBER(S) ESC-TR-2007-067	
12. DISTRIBUTION / AVAILABILITY STATEMENT Approved for public release; distribution is unlimited.					
13. SUPPLEMENTARY NOTES					
14. ABSTRACT Previously, a novel formulation for the generation of three-dimensional (3D) inverse synthetic aperture radar (ISAR) images based on recent developments in high resolution spectral estimation theory was presented. Because this technique requires only "snapshots" of data, where a "snapshot" is defined as a block of Nyquist sampled frequency-time pulses of data, we refer to it as "3D snapshot imaging." Concomitant with these results, recent advances in interferometric SAR imaging have demonstrated the use of two-dimensional (2D) range-Doppler image phase information to extract "out-of-plane" height information to obtain 3D images of ground scenes. In this case, a unique sampling grid is generated that allows "overlaying" of nearly identical 2D range-Doppler images and uses phase differences between these images to estimate the "out-of-plane" height information, from which a 3D image is developed. In this report, we develop a framework connecting these two techniques, particularly applicable to forming 3D images of target types typically dominated by smaller numbers (<20) of scattering centers, and characterized by deterministic exoatmospheric motion having torque-free Euler dynamic spin and precession. Applications of the development are illustrated using simulation data; specifically, the wideband, monostatic field is simulated using a simple point scatter model of a generic cone-like target, and the phase-enhanced 3D image is generated for differing cases. Extensions of the technique to bistatics are also discussed.					
15. SUBJECT TERMS					
16. SECURITY CLASSIFICATION OF:			17. LIMITATION OF ABSTRACT Same as report	18. NUMBER OF PAGES 37	19a. NAME OF RESPONSIBLE PERSON
a. REPORT Unclassified	b. ABSTRACT Unclassified	c. THIS PAGE Unclassified			19b. TELEPHONE NUMBER (include area code)